Development of a Mixed Halide-chalcogenide Bismuth-based Perovskite MABiI$_2$S with Small Bandgap and Wide Absorption Range

Chu Zhang[a], Siowhwa Teo[a], Zhanglin Guo[a], Liguo Gao[b], Yusuke Kamata[a], Zhenhua Xu[a], Tingli Ma [a,*]

a Graduate School of Life Science and Systems Engineering, Kyushu Institute of Technology, Kitakyushu, Fukuoka, 808-0196, Japan

b School of Petroleum and Chemical Engineering, Dalian University of Technology, Panjin Campus, Panjin 124221, P. R. China;

Abstract: During the last years, the lead perovskites have achieved high power conversion efficiency of 23%. However, its long-term stability and toxicity are still the crucial issues that required attention. In this study, we are the first to report on the synthesis and characterizations of a new lead-free mixed halide-chalcogenide perovskite MABiI$_2$S (MBIS), and determined its physical and optical properties by various testing methods. The MBIS has a low bandgap of 1.52 eV, with an extended absorption onset up to over 1000 nm. Solar cells fabricated with the MBIS were inspected and device improvement were applied.

Keywords: Lead free perovskites, Bismuth-based perovskite, Small bandgap.

The rapid development of lead-based halide perovskite solar cell has brought forth to astonishing power conversion efficiency (PCE) of 23.3% [1]. No doubt that the lead-based halide perovskites are unique light absorbers, coupled with amazing wide absorption range [2], long carrier diffusion length [3], high quantum conversion ratio [4], small direct bandgap, and good defect tolerance ability [5]. However, the lead-based perovskites also encountered major disadvantages such as the instability in a humid environment and the toxicity of the Pb2+ generated by the irreversible decomposition [6-7]. These issues impede the commercialization and practical usage of the perovskite solar cell.

In order to overcome the disadvantages of the lead-based perovskites, a valid idea is to partially or fully replace the lead element with environmental friendly elements, such as tin, bismuth, germanium, copper, and alkaline-earth metals (Ba, Sr, Ca). However, not all the attempts were successful: Sn2+ and Cu2+ were proved to be unstable and toxic, while Ge2+ and the alkaline-earth metals exhibit larger bandgaps which are disfavoring for solar cells application [8-12].

Among these potential lead-free substituents, bismuth is highly preferable owing to its low trap state densities, long carrier lifetime and proper defect tolerance ability [13-15] as predicted from computational scanning and experimental studies, and more importantly, bismuth is much less toxic than lead [16]. Despite bismuth perovskite exhibited exciting progression, major problems of the bismuth perovskites have been revealed as well. Bismuth halide perovskite would crystalize into a 2D hexagonal layered phase, which promotes intrinsic defect sites [17]. Another issue is that bismuth perovskites tend to have large and indirect bandgap near 2.0 eV, which is not very suitable for perovskite solar cells [18].

Whilst, bismuth chalcogenides, such as Bi$_2$S$_3$ and Bi$_2$Se$_3$, were reported to have smaller bandgaps than that of the bismuth halide perovskites, and these materials are also stable and non-toxic [19-21]. The incorporation of the chalcogenide anions to the halide bismuth perovskites could reduce their bandgaps without affecting its optoelectronic properties. Another potential advantage of incorporating of the chalcogen anions is that the Bi-chalcogen bond is more covalent than the Bi-halogen bond, which resulted in higher overall covalence magnitude of the compound, thus brought forth to higher stability [22]. Evidently, computational predictions indicated that the mixed chalcogen-halogen perovskite existed in a steady form [23], which merited the photovoltaic development.

In this work, we successfully synthesized a novel and high crystallinity MABiI$_2$S (MBIS) lead-free mixed chalcogen-halogen perovskite via a two-step solid-state reaction process. In this manuscript, we provided an in-depth analysis to elucidate the composition of MBIS powder via various methods. The MBIS possesses small bandgap with large absorption range. Based on these fine properties, we further explored the photovoltaic performances of the MBIS solar devices. Although the devices achieved low PCE at this stage, several enhancement routes are suggested. It can be expected that with further optimized fabrication techniques, the MBIS surely can be a promising lead-free perovskite material.

Since the MBIS perovskite is a new material without any presentation of previous report, we start our discussion with the calculation of the Gold-Schmidt tolerance factor (t) and the octahedral factor (μ) [24].Corresponding ionic radii of all the ions were chosen from Shannon's effective ionic radii [25]: r(MA) = 1.800, r(Bi) =1.030, r(S) = 1.840. and r(I) = 2.200. Theoretically, a halide perovskite recorded t and μ in the range of 0.81 to 1.11 and 0.44 to 0.90, respectively [26]. While experimentally and in accordance to the equations (1) and (2), the calculated t and μ recorded a value of 0.853 and 0.495, respectively, which is in great agreement with the literature. In our case, t < 0.9 implies the MBIS perovskite would possibly prefer an orthorhombic or rhombohedral lattice instead of a cubic lattice. While the calculated μ indicates that the MBIS perovskite is hypothesized to be in 3D crystal structure.

The MBIS powder sample was synthesized by a two-step solid-state reaction, as shown in Figure S1. The final product of the solid-state synthesis MBIS was a dark brown powder, the chemical process can be described below.

After the first step solid-state synthesis, a distinct phase of BiIS was formed.

$$Bi_2S_3 + BiI_3 \xrightarrow{180℃} 3BiIS \qquad (1)$$

After the second step of the solid-state annealing, we can see that the characteristic peaks of the BiIS disappeared, while the target phase of MBIS appeared.

$$BiIS + MAI \xrightarrow{150℃} MABiI_2S \qquad (2)$$

Figure 1. shows the SEM images of the MBIS perovskite, in which the MBIS perovskite grew in a fine 3D nanoparticles of ca. 50 nm.
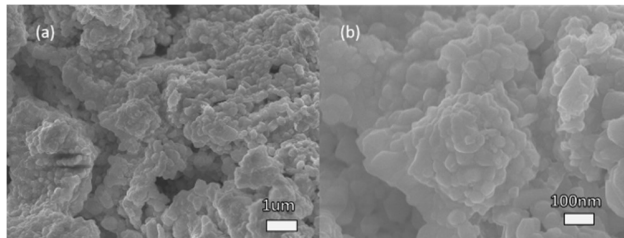
Fig. 1 SEM images of the MABiI$_2$S sample. (a) Image for the overall view of the powder sample. (b) The close look of the nanoparticles.

The composition of the as-prepared powder sample was determined through XRD. As MBIS is a newly synthesized material, there has no standard PDF card for the MBIS perovskite. We thus compared the XRD pattern of our sample to a simulation result of MASbI$_2$S [27]. Owing to the Sb and Bi elements are of the same family, the XRD pattern is predicted to be similar, with only a small shift of certain peaks. As shown in Figure. 2, all main peaks of the MBIS perovskite is consistent with the simulated pattern. Comparing the XRD patterns of our as-synthesized MBIS against the reference MASbI2S pattern [27], the XRD peaks located at 21.1 °, 25.0 °, 26.1 °, 30.5 °. 31.0 °, 34.2 °, 35.1 °, 36.9 °, and 37.8 ° were shifted to higher 2θ value by about 0.8 ° due to the replacement of larger Bi atom over the Sb. It is notable that the crystal plane distance is inversely proportional to the diffraction angle, in which peak shifting takes place when a smaller Sb atom is replaced by a larger bismuth atom. However, an impurity phase Bi$_2$S$_3$ was also found to exist (marked as red stars) within the perovskite material owing to incomplete conversion of the Bi$_2$S$_3$ during the solid-state reaction.
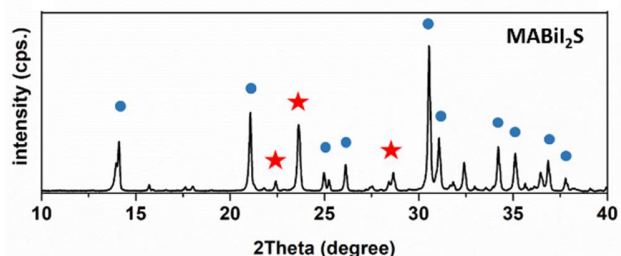
Fig. 2 XRD pattern of the MBIS perovskite. The main phase is marked by the blue dots, impurity phase Bi$_2$S$_3$, is marked by the red stars.

To further confirm the composition of our sample, EDX detecting and elemental mapping were performed, as shown in Figure 3. The presence of all expected elements are revealed from the EDX spectrum(Figure 3 (a)), where strong bismuth and iodine signals are observed, indicative of the higher proportion of bismuth and iodine over the other elements. From the elemental atomic percentage yielded from the EDX pattern, we can determine that the atomic ratio of the bismuth, sulfur and iodine elements are approximately 1:1:5. This ratio implies sulfur loss during the solid-state reaction process. Our observation also agrees with this conclusion, where a small amount of yellow solid, which was proven to be sulfur, was collected from the lid of the solid-state reaction container.

However, we should aware that the EDX elemental ratio is only a qualitative estimation, thus it is still necessary to determine the actual formula of our material with additional precise means.
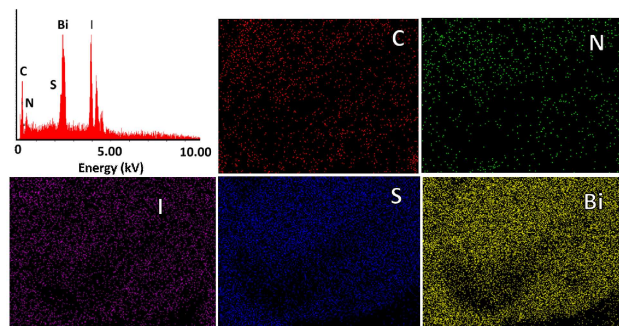
Fig. 3 (a) The EDX pattern and (b)-(f) the elemental mapping images of the MBIS perovskite. Each element is marked on the corresponding mapping image.

Figure 3 (b)-(f) show the elemental mapping images of the as-prepared MBIS sample. Corresponding elements were marked on their mapping images. It is observed that all the elements were distributed evenly in the mapping area, indicating that the sample was in a homogenous state. We inferred that since the sulfur element does not aggregate and it follows the distribution pattern of other elements, the amount of Bi2S3 impurities presence in this sample is insignificant.

The chemical states of each element in the MBIS perovskite were elucidated through the XPS profile. As shown in Figure 4, the wide scan of the as-prepared MBIS perovskite proved the presence of all the expected elements of the MBIS perovskite and all the dominant binding orbitals of each element were revealed. By identifying the dominating orbitals from the spectrum and inspect the narrow scan of Bi, S and I, we are able to decide the valence of each element, where Bi is 3+, S is 2- and I is 1-. The narrow scan of the iodine were shown in Figure S3. Especially, the narrow scan of the S 2p peak located at 163.5 eV, which is attributed to the metal-sulfur bond of 2- valence. The peak of 0-valence sulfur element did not appear, suggesting that no residue sulfur remained after the entire solid-state reaction process. This also supported our conclusion that the sulfur has been incorporated to into the bismuth perovskite and the MBIS is successfully synthesized.

In order to evaluate the light absorption ability of the MBIS, we recorded its UV-Vis spectra. Fig.5 (a) shows the UV-Vis absorption spectrum of the MBIS powder sample. From this figure, we can see that the MBIS perovskite started to show optical absorption from 350 nm, and has a strong absorption intensity in the range of 350 – 700 nm. Its absorption edge extended to 750 nm while still maintain a half of the maximum absorption intensity. We can conclude that the MBIS perovskite shows very promising light absorbing potential, showing high absorption and large absorbing range in the visible light range that is comparable to the Pb-based perovskites. It is worth noting that the MBIS perovskite showed proper absorbing ability in the infrared region of the solar spectrum, extending its absorption range up to over 1000 nm. The special absorption range would not only be beneficial to the single-junction solar

cell application, but also be beneficial to the multi-junction device application.
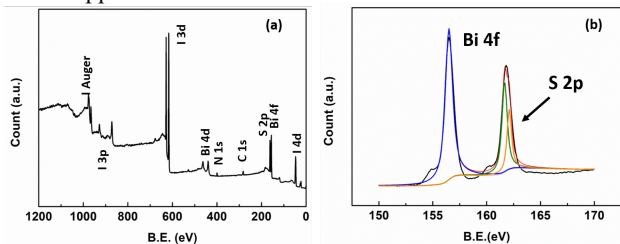
Fig. 4 (a) The full range survey XPS spectrum of the MBIS perovskite and (b) narrow scan of Bi 4f orbital and S 2p orbital. All the peaks and the corresponding orbital for the component elements were marked out.

From the UV-Vis absorption spectrum, we can constructed the Tauc' plot following the relation below, and estimated the bandgap of the MBIS perovskite. By extrapolation we can obtain the optical bandgap of the MBIS to be $E_g = 1.52$ eV. This is a very promising bandgap value for the photovoltaic devices. Judging by the optical properties above, we can confidently apply this new perovskite material to the solar cell device.
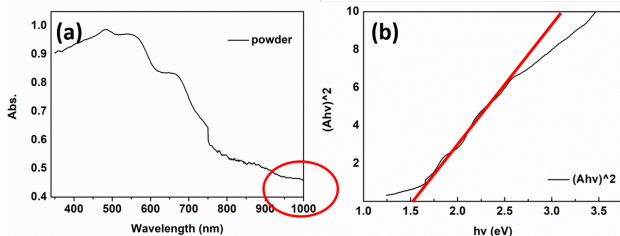
Fig. 5 (a) UV-vis powder absorption spectrum of the MBIS perovskite showing an absorption range reaching 1000 nm. (b) The Tauc' plot derived from the UV-Vis absorption spectrum of the MBIS.

The solubility of the MBIS perovskite in various solvents such as IPA, ethanol, chlorobenzene, and DMF was tested (Figure S4 (a)). When the MBIS dissolved in solvents with low polarity, the solutions showed significant lamination phenomenon. It is also worth noting that ethanol and IPA would damage the solute, forming unknown green solid, which is most probably an organic bismuth compound [28]. It is obvious that we should choose DMF as the solvent. After filtering, the DMF solution appeared to be a clear dark red solution as shown in Figure S4 (b). Films fabricated on FTO substrate with and without mesoporous scaffold layer were shown in Figure S4 (c). These films are thin and highly transparent, which are non-suitable for perovskite solar cells. We have tried to increase the concentration of the precursor solution, to slow down the spin coating speed, or to fabricate multi-layered films, aiming at achieving thicker MBIS film. However, neither of these routes could fulfill our goal. As expected, the cells fabricated with these highly transparent films yielded no PCE. Apparently, the spin-casting method is not valid here.

In order to solve the film formation problem, we introduced an in-situ growth process using a CBD deposition method to coat the Bi_2S_3 nanoparticles [29]. A sequential spin coating of the BiI3 film, and an MAI vapor assisted in-situ solid-state annealing growth were then applied to get the target MBIS perovskite film, as illustrated in Fig S2 and described in the experimental section. Through this process, dark brown MBIS

films were fabricated and the composition of the films were verified by XRD for each layer. The XRD pattern (Figure S6) displayed that Bi_2S_3 existed throughout the fabrication process. Bi_2S_3 was reported to possess a narrow bandgap and its bandgap can be significantly affected by the morphology and particle size [30]. However, it was also demonstrated that the Bi_2S_3 could display high conductivity [31]. In our devices, it is very plausible that these nanoparticles can be potential defect sites that cause leakage.

To test the performance of the MBIS perovskite solar cells, we assemble the devices whose structure can be described as [FTO/c-TiO2/m-TiO2/MBIS/PCPDTBT/Au]. Initially the as prepared devices show low PCE of 0.01%. Surely, we should enhance the device. Starting from the top layer of the device, we found that the gold electrode was not as compact as we expected. It is reasonable to predict that the surface of the MBIS would not be as smooth as that of the lead-based perovskite, thus a surface treatment agent should be introduced. By applying PEDO:PSS as the surface treatment agent, we observed that the gold electrode became smoother and much more compact, as shown by the inset photos of the devices with and without the PEDOT:PSS treatment. The J_{SC} of the device increased significantly, from 0.40 mA.cm^{-2} to 1.03 mA.cm^{-2}. Another method we employed is to apply dynamic spin coating with the BiI3 layers, which further enhanced the quality of the MBIS layer and increased the J_{SC} to over 2.0 mA.cm^{-2}, with an increased FF from 0.25 to 0.30.

Another issue is the HTM. The PCPDTBT was chosen due to it can form fine-quality film on rougher surfaces. However, the device utilizing the PCPDTBT only yield $V_{OC} = 0.1$ V. From Figure 7 (b) we can see that the band mismatch of the PCPDTBT is much more severe than the Spiro-OMeTAD, resulting in significant V_{OC} loss. On the other hand, the Spiro-OMeTAD form poor film on top of the MBIS. Also, the water-based surface passivation agent PEDOT:PSS will damage the Spiro-OMeTAD, reducing its hole extraction ability. Applying the Spiro-OMeTAD as the HTM would resulting in a significant increase of V_{OC} from 0.1 V to 0.22 V, but the J_{SC} was simultaneously decreased from 2.2 mA.cm^{-2} to 1.96mA.cm^{-2}. Table 1 below summarized the champion performances of the devices before and after enhancements.

Table 1. Device performance before and after enhancements.

Treatment	PCE	V_{OC}	J_{SC}	FF
After	0.13	0.22	1.96	0.30
Before	0.01	0.10	0.43	0.25

Another interesting phenomenon to point out is that when we intentionally fabricate the device based a damaged mesoporous TiO2 scaffold (showed in Figure S5), the reduction of the I-V performance is surprisingly small. As listed in the table S1, the defected cell displayed a small reduction of each parameter compared to the well-fabricated control cell. This indicated that the MBIS perovskite possesses high defect tolerance ability, which is an important criterion for real-life scenario of the perovskite solar cell applications. It was also noticed that the mesoporous TiO_2 film with CBD Bi_2S_3 layer on

top was damaged much faster than a plane m-TiO$_2$ film, even when stored in the glovebox, which indicates that the CBD process would be harmful to the m-TiO$_2$ scaffold, since the CBD process were carried out in water-based system and normally at acidic environment. Alternative CBD method that can deposit Bi$_2$S$_3$ film without the help of m-TiO2 layer or without water/acid could greatly enhance the device performance.
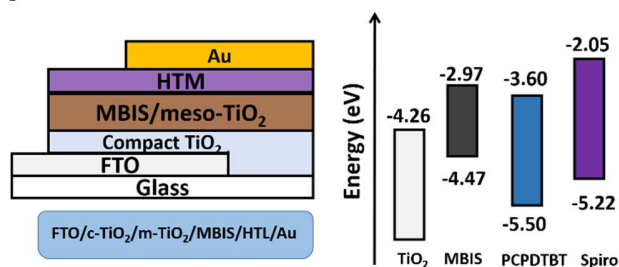
Fig.7 Sketch of the (a) devices structure and (b) The band positions.

In summary, we have successfully synthesized a mixed chalcogen-halogen lead-free perovskite MBIS via a simple two-step solid-state synthesis. Based on the UV-Vis absorption, we determined that the MBIS perovskite has a bandgap of 1.52 eV, and it possesses a wide absorption range that extends to over 1000 nm. The unique properties of this material meet the criterion for the photovoltaic application. By employing an in-situ growth technique, we have successfully solved the film quality issue of the MBIS where the treated MBIS device showed PCE enhancement over the untreated device due to the poor perovskite film formation on the TiO2 substrate. Several enhancement route were suggested and the PCE of the device were increased from 0.06% to 0.13%. In addition, this material displayed high defect tolerance ability. The special properties of the MBIS perovskite show that it can be a viable light absorber with refined device fabrication techniques.

Acknowledgments

Reference

[1]. Yang Y, You J, Lei M, inventors. The Regents of the University of California (Oakland, CA, US), assignee. Efficient and Stable Perovskite Solar Cells with All Solution Processed Metal Oxide Transporting Layers. United States Patent 0033983. 2018-02-01.

[2]. Lee M. Teuscher J. Miyasaka T. Murakami T. Snaith H. *Science.* 2012 Nov 02;338(6107):643-647.

[3]. Dong Q. Fang Y. Shao Y. Mulligan P. Qiu J. Cao L. et al *Science.* 2105 Feb 27;347(6225):967-970.

[4]. Yang B. Dyck O. Poplawsky J. Keum J. Puretzky A. Das S. et al. *J Am Chem Soc.* 2015 Jul 9;137(29):9210–9213.

[5]. Brandt R. Stevanovic V. Ginlev D. Buonassisi T. *MRS Commun.* 2015;5:265−275.

[6]. Berhe T. Su W. Chen C. Pan C. Cheng J. Chen H. et al. *Energy Environ Sci.* 2015 Oct 20;9:323-356.

[7]. Feng J. Xiao B. *J Phys Chem C.* 2014 Aug 6;118(34):19655-19660.

[8]. Noel N. Stranks S. Abate A. Wehrenfennig C. Guarnera S. Haghighirad A. et al. *Energy Environ Sci.* 2014 May 01;7:3061-3068.

[9]. Park B. Philippe B. Zhang X. Rensmo H. Boschloo G. Johansson E. *Adv Mater.* 2015 Sep 29;27(43):6806-6813.

[10]. Krishnamoorthy T. Ding H. Yan C. Leong W. Baikie T. Zhang Z. et al. *J Mater Chem A.* 2015 Oct 16;3:23829-23832.

[11]. Cui X. Jiang K. Huang J. Zhang Q. Su M. Yang L. et al. *Synthetic Metals.* 2015;209:247-250.

[12]. Pazoki M. Jacobsson T. Hagfeldt A. Boschloo G. Edvinsson T. *Physical Review B.* 2016 Apr 07;93:144105.

[13]. Zhou H. Chen Q. Li G. Luo S. Song T. Duan H. et al. *Science.* 2014 Aug 01;345(6196):542-546.

[14]. Johansson MB. Zhu H. Johansson EMJ, *J Phys Chem Lett.* 2016;7(17):3467-3471.

[15]. Hoye RLZ. Brandt RE. Osherov A. Stevanovic V. Stranks SD. Wilson MWB. et al. *Chem Eur J.* 2016 Feb 18;22(8):2605-2610.

[16]. Hebig J, Kuhn I, Flohre J, Kirchartz, T. *ACS Energy Lett.* 2016 Jun 21;1(1):309-314.

[17]. Eckhardt K, Bon V, Getzschmann J, Grothe J, Wisser FM, Kaskel S. *Chem Commun.* 2016 Jan 19;52:3058-3060.

[18]. Murugan V. Ohta T. Iikubo S. Kapil G. Ripolles TS. Ogomi Y. Ma T. Pandy SS. Shen Q. Toyoda T. Yoshino T. Minemoto T. Hayase S. *Chem Mater.* 2016;28(18):6436-6440.

[19]. Chang JA, Rhee JH, Im SH, Lee YH, Kim HJ, Seok SI, et al. *Nano Lett.* 2010 Jul 14;10(7):2609-12.

[20]. Choi YC, Lee DU, Noh JH, Kim EK, Seok SI. *Adv Funct Mater.* 2014 Mar 03;24(23):3587-3592.

[21]. Martinez L, Bernechea M, Garcia deArquer FP, Konstantatos G. *Adv Ener Mater.* 2011 Sep 19;1(6):1029-1035.

[22]. Hong F, Saparov B, Meng W, Xiao Z, Mitzi DB, Yang Y. *J Phys Chem C.* 2016, Mar 9;120(12):6435−6441.

[23]. Goldschmidt V. M. Die Gesetze der Krystallochemie. *Naturwissenschaften.* 1926. 14:477.

[24]. Shannon R,. *Acta Cryst.* 1976, A32:751-767.

[25]. Li C, Lu X, Ding W, et al. *Acta Crystallogr B.* 2008 Nov 14;64(6):702-707.

[26]. Nie R, Mehta A, Park B, Kwon HW, Im J, Seok SI *J Am Chem Soc.* 2018 Jan 4;140(3):872–875.

[27]. Ng C. Lim H. Hayase S. Zainal Z. Shafie S. Huang N. *Ind Eng Chem Res.* 2018 Jan 23;57(6):2146-2154.

[28]. Dessy R, Kitching W. *J Am Chem Soc.* 1966 Feb;88(3):467-470.

[29]. Moreno-Garcia H, Nair MTS, Nair PK. 2011. 519(7):2287-2295.

[30]. Bernechea M, Cao Y, Konstantatos G. *J Mater Chem A.* 2015 Aug 31;3:20642-20648.

[31]. Liufu SC, Chen LD, Yao Q, Wang CF. *J Phys Chem B.* 2006 Nov 3;110(47):24054-240.

The graphic abstract